MATERIALS SCIENCE

Selective area doping for Mott neuromorphic electronics

Sunbin Deng[1]†‡*, Haoming Yu[1]†, Tae Joon Park[1]†§*, A. N. M. Nafiul Islam[2], Sukriti Manna[3,4], Alexandre Pofelski[5], Qi Wang[1], Yimei Zhu[5], Subramanian K. R. S. Sankaranarayanan[3,4], Abhronil Sengupta[2], Shriram Ramanathan[1]‖*

The cointegration of artificial neuronal and synaptic devices with homotypic materials and structures can greatly simplify the fabrication of neuromorphic hardware. We demonstrate experimental realization of vanadium dioxide (VO_2) artificial neurons and synapses on the same substrate through selective area carrier doping. By locally configuring pairs of catalytic and inert electrodes that enable nanoscale control over carrier density, volatility or nonvolatility can be appropriately assigned to each two-terminal Mott memory device per lithographic design, and both neuron- and synapse-like devices are successfully integrated on a single chip. Feedforward excitation and inhibition neural motifs are demonstrated at hardware level, followed by simulation of network-level handwritten digit and fashion product recognition tasks with experimental characteristics. Spatially selective electron doping opens up previously unidentified avenues for integration of emerging correlated semiconductors in electronic device technologies.

INTRODUCTION

Neuromorphic computing represents a computational paradigm that aims to emulate characteristics of information processing in the brain. Mott semiconductors offer a powerful platform to realize neuromorphic hardware via electrically driven conductance transitions (*1*–*3*). For instance, a single vanadium dioxide (VO_2) device connected to a capacitor can serve as an oscillatory artificial neuron in a more compact manner (*4*–*7*) compared to traditional silicon (Si) complementary metal-oxide semiconductor layouts. While individual artificial neurons and synaptic primitives have been demonstrated with correlated electron semiconductors demonstrating substantial potential (*8*–*13*), interconnected networks made of neurons and synapses at hardware level and relevant fabrication processes for Mott circuits are in their infancy. While implementation of hardware-based neuromorphic test structures have been reported in literature (*14*–*16*), the interconnected neuronal and synaptic components usually adopted heterotypic material systems and device structures.

We hypothesize that the ability to perform multiple neural functions with the same material system can simplify the chip-scale fabrication process among other benefits. Especially when new materials that have never been introduced in a fab are being considered, if they can offer more than one compelling device application within the same technology domain, then the chances of their consideration naturally become greater. However, this requires innovation in the implementation of diverse neural functions into identical devices after fabrication. For this purpose, we borrow the concept of selective doping from integrated circuit industry and apply them to quantum materials. Selective area doping, which is effective not only for traditional semiconductors (e.g., Si and III-V compounds) but also for emerging materials [e.g., two-dimensional materials (*17*–*19*)], is used across the spectrum of semiconductor technologies to create solid-state devices, such as junctions, contacts, transistors, and inversion layers. Adapting this approach to Mott semiconductors represents a promising direction.

At the outset, we note that there are profound differences in doping physics between band semiconductors such as Si and Mott semiconductors such as VO_2 (*20*). In Si and related materials, aliovalent doping concentration in the order of parts per million is sufficient for repositioning the Fermi level or band edges for function, whereas in Mott materials, doping density in the order of 0.1 to 1 electron per unit cell (i.e., ~10^5 to 10^6 larger doping density) is needed to induce conductance changes (*21*, *22*). Hence, strategies for doping Mott semiconductors that can be scalable and viable for semiconductor technologies are a nontrivial problem.

The principal objective of this study is to experimentally demonstrate the cointegration of artificial neuronal and synaptic components with homotypic material systems and device structures on chip by spatially selective hydrogen donor doping of VO_2. This is demonstrated by careful design of catalytic and inert electrode pairs and experimental measurements of electrical properties. Hydrogen as a dopant (*23*–*25*) performs two important and unique functions here: reduces the insulating ground-state resistance and controls the memory state retention (i.e., volatility versus nonvolatility) in two-terminal Mott devices. Hydrogen is selectively doped using catalytic metal electrodes (e.g., Pd), such that the hydrogenated devices can serve as synapses for learning and memory, while pristine undoped devices can function as neurons for signal

[1]School of Materials Engineering, Purdue University, West Lafayette, IN 47907, USA. [2]School of Electrical Engineering and Computer Science, The Pennsylvania State University, University Park, PA 16802, USA. [3]Center for Nanoscale Materials, Argonne National Laboratory, Lemont, IL 60439, USA. [4]Department of Mechanical and Industrial Engineering, University of Illinois, Chicago, IL 60607, USA. [5]Department of Condensed Matter Physics and Materials Science, Brookhaven National Laboratory, Upton, NY 11973, USA.
†These authors contributed equally to this work.
‡Present address: School of Electrical and Computer Engineering, Georgia Institute of Technology, Atlanta, GA 30318, USA.
§Present address: Department of Materials Science and Engineering, University of California, Berkeley, Berkeley, CA 94720, USA.
‖Present address: Department of Electrical and Computer Engineering, Rutgers, The State University of New Jersey, Piscataway, NJ 08854, USA.
*Corresponding author. Email: deng256@purdue.edu (S.D.); park1080@purdue.edu (T.J.P.); shriram@purdue.edu (S.R.)

transfer. Therefore, by spatially selective doping, we are able to realize the two most sought-after neuromorphic functions essential for neural networks with the same parent material. The gentle forming gas (5% H_2) anneal process causes no lattice damage, and both ground-state resistance and volatility of the memory are tunable. By suitable lithographic design of catalytic and inert electrodes, both volatile and nonvolatile devices with homotypic materials and structures can be integrated on a single chip (Fig. 1, A and B). As proof of principle, neural circuit motifs are then fabricated and demonstrated at hardware level to emulate excitation/inhibition functions. With the experimental characteristics, network-level recognition tasks are further simulated on the Modified National Institute of Standards and Technology (MNIST) (*26*) and Fashion-MNIST (*27*) datasets with test accuracies comparable to other state-of-the-art unsupervised approaches (Fig. 1, C and D).

RESULTS

Spatially selective hydrogenation of VO_2

VO_2 can be hydrogen-doped via a variety of methods, such as high-temperature annealing (*28*), electrochemical insertion (*10*, *29*), and catalytic spillover (*23*, *24*). This work uses the catalytic spillover method to demonstrate selective doping, which occurs at back-end compatible low process temperatures (fig. S1). Palladium (Pd) is a commonly used catalytic electrode in hydrogen spillover process (*30*), and it is also effective toward catalytic hydrogen doping of VO_2 (*31*, *32*). The inserted hydrogen dopants (i.e., protons) occupy interstitial sites among VO_2 lattices and bond with oxygen atoms along with electron transfer (Fig. 2A and fig. S2). The electron doping effect can be observed in the vanadium $L_{2,3}$ and oxygen K-edges from the electron energy loss spectra in Fig. 2B and fig. S3. The relative intensity ratio of t_{2g} peak over e_g peak in hydrogenated VO_2 (H_xVO_2) is much decreased compared with that in pristine VO_2, indicating that more states at the lower t_{2g} level are filled by electrons. Meanwhile, the vanadium $L_{2,3}$ edge shows a red shift, which is consistent with the valence state change from V^{4+} to V^{3+} as a result of higher V 3d orbital occupancy (*33*). X-ray diffraction (XRD) spectra (Fig. 2C) also reflect the Pd catalyst–assisted hydrogen spillover process. A 50-nm-thick pristine VO_2 thin film has a monoclinic $(020)_M$ peak at 39.8° [equivalent to a rutile $(200)_R$ peak] at room temperature. After the hydrogenation with Pd electrodes, the diffraction peak of $(200)_R$ shifts to 36.2°, indicating the out-of-plane lattice expansion (*23*).

Compared with the Pd electrode, the TiAu electrode is less active in the hydrogen spillover process (*34*). The VO_2 film with the TiAu electrodes remains identical in its XRD spectrum after the hydrogenation, and the region near TiAu is still in its original gray color (indexed as VO_2) (fig. S4). It indicates that negligible doping occurs at the TiAu-VO_2-H_2 triple-phase boundary. Therefore, by selecting the combination of catalytic (Pd) and inert (TiAu)

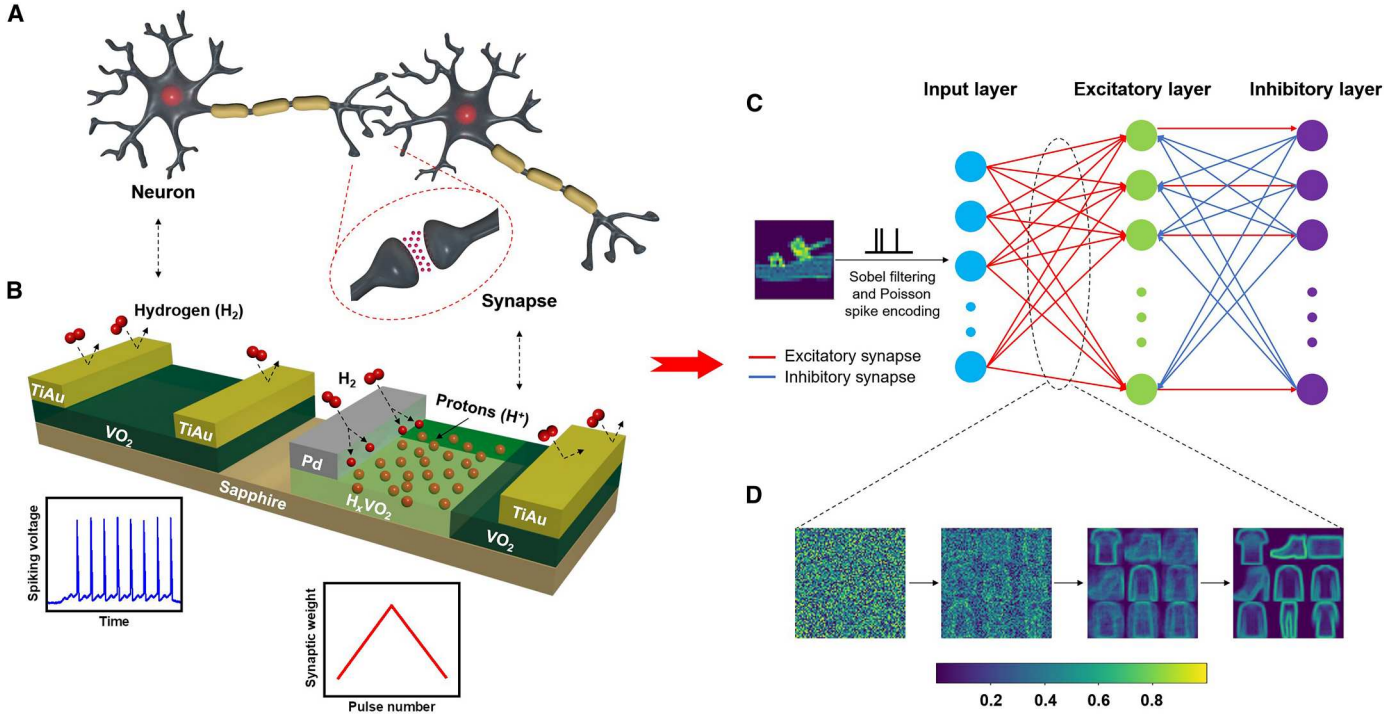

Fig. 1. Homotypic Mott neuromorphic platform. (**A**) Schematic of biological neurons and synapses. Neurons serve as processing units connected through synapses. (**B**) Schematic of two-terminal volatile and nonvolatile $(H_x)VO_2$ devices integrated on a single sapphire substrate. The volatilities in the $(H_x)VO_2$ material system can be controlled by selective hydrogenation. Pristine vanadium dioxide (VO_2) devices can be used as spiking neurons, and nonvolatile H_xVO_2 devices can serve as analog synaptic components. (**C**) Network architecture for the $(H_x)VO_2$ spiking neural network (SNN) proposed in this work. An example input is from the Fashion-MNIST (Modified National Institute of Standards and Technology) dataset, and it goes through Sobel filtering and Poisson spike encoding before being fed into the network. For MNIST, only the spike encoding is performed before being input to the network. The input layer size is 784, followed by 400 excitatory and inhibitory neurons (1600 for MNIST). (**D**) Weight evolution during training on Fashion-MNIST of nine representative neurons of the network. The weights are modulated according to the spike timing–dependent plasticity (STDP) rule and approximate different patterns in the training set.

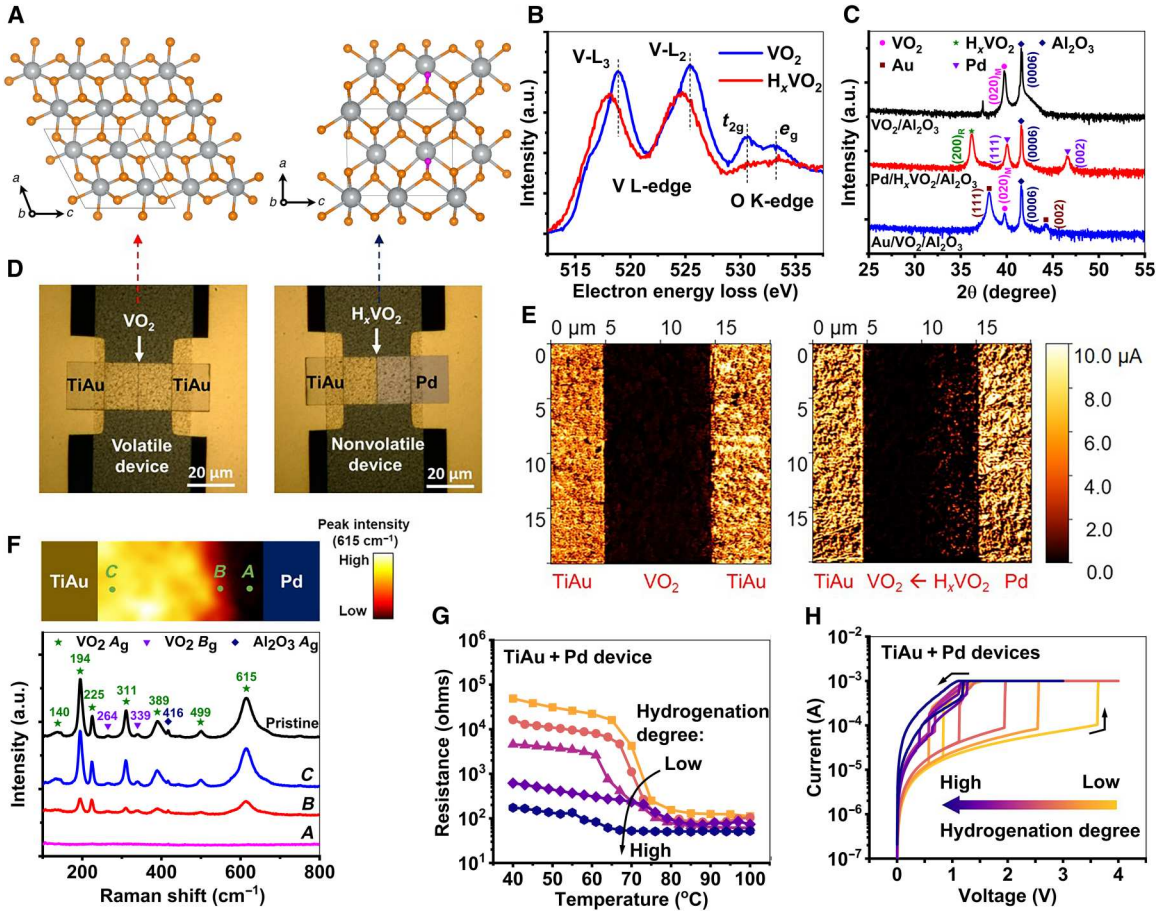

Fig. 2. Selective area carrier doping. (**A**) Crystal structures of VO_2 and H_xVO_2. Gray, orange, and purple spheres stand for vanadium, oxygen, and hydrogen atoms, respectively. The pristine VO_2 has a monoclinic structure at room temperature. In H_xVO_2, hydrogen atoms tend to occupy interstitial sites among VO_2 lattices. Density functional calculations show that H_xVO_2 stays in a pseudorutile phase when the hydrogenation level (x) is >0.25. (**B**) Averaged electron energy-loss spectroscopy spectra from a VO_2 and a H_xVO_2 region centered on the vanadium (V) $L_{2,3}$ and oxygen (O) K-edges. The spectra were normalized using the averaged intensity level between 640 and 660 eV (see fig. S3). a.u., arbitrary units. (**C**) X-ray diffraction (XRD) spectra of the VO_2 thin film (black line) grown on c-plane sapphire substrate, the H_xVO_2 with Pd electrodes (red line), and VO_2 with TiAu electrodes (blue line) after the hydrogenation. The out-of-plane lattice of VO_2 after the hydrogenation is expanded. (**D**) Optical microscope image of pristine and H-doped VO_2 devices was fabricated on a single substrate. The channel region is noted with a down pointing arrow. (**E**) Conductive atomic force microscope (C-AFM) images of the $(H_x)VO_2$ channels with different electrode combinations after the hydrogenation. Bright conductivity contrast appears near the Pd electrode of TiAu + Pd device, indicating the hydrogenated VO_2. (**F**) Spatial Raman mapping in the $(H_x)VO_2$ channel of TiAu + Pd device (top panel). The Raman peak of VO_2 at 615 cm^{-1} was fixed for this mapping. This characteristic peak exists in VO_2 but disappears in H_xVO_2. Raman spectra measured at points *A*, *B*, and *C* (bottom panel). The Raman spectrum of monoclinic VO_2 is plotted as a reference. (**G**) Temperature-dependent resistance of the TiAu + Pd device was annealed at different annealing conditions. (**H**) Current-voltage relation (*I-V*) curves of the TiAu + Pd device for different hydrogenation levels. Hydrogenation can effectively create intermediate resistance states in VO_2.

electrodes, proton distribution across the device channels in two-terminal VO_2 devices (Fig. 2D) can be controlled. To visualize the proton distribution, the surface current of devices with different electrode pairs were probed using a conductive atomic force microscope (C-AFM) after the hydrogenation (fig. S5). For the VO_2 device with two inert TiAu electrodes (i.e., TiAu + TiAu device), the probed current in the channel shows low intensity, indicating an insulating nature of VO_2 and that no protonation occurred during the hydrogenation. In contrast, for the VO_2 device with Pd electrodes (i.e., Pd + Pd device), the probed current becomes higher, indicating proton distribution across the whole channel. The Pd + Pd device shows metallic H_xVO_2 behavior, where both thermally and electrothermally driven insulator-metal transition phenomena are not observed (figs. S6 and S7). Here, we refer to electrothermally driven insulator-metal transition as E-IMT. For the device with an asymmetric electrode pair (i.e., TiAu + Pd device), the probed current decreases monotonically across the channel from Pd to TiAu electrodes, as shown in Fig. 2E. The proton distribution was further mapped using Raman spectroscopy. All the peaks observed in the channel are in good agreement with the reported monoclinic VO_2 results (*35*). On the other hand, the metallic rutile H_xVO_2 has no Raman peaks in this range (100 to 800 cm^{-1}) (*36*). Thus, by comparing the intensity of characteristic VO_2 peak (at 615 cm^{-1}) measured at different locations within the channel, a decrease of proton density across the channel from Pd to TiAu was observed, indicating a transition from H_xVO_2 to VO_2 (Fig. 2F and fig. S8). By subtly controlling hydrogenation level and proton distribution, more intermediate states are

accessible. Figure 2G shows temperature-dependent resistance of the device with asymmetric electrode pairs at different hydrogenation levels. The ground-state resistance continues to decrease with increase of hydrogenation time and eventually becomes comparable to the resistance after the phase transition. The hydrogenation also tunes the electrothermally driven transition behavior of H_xVO_2 device (Fig. 2H and fig. S9). Depending on the hydrogen doping, threshold voltage (V_{th}) for triggering the E-IMT decreases from ~3.6 to ~0.6 V. Further hydrogenation can induce a nonvolatile current-voltage relation (I-V) hysteresis characteristic of the device. Such a nonvolatility is reversible, and the volatile E-IMT phenomenon is reproducible in dehydrogenated devices (fig. S10).

Volatile and nonvolatile memory in $(H_x)VO_2$ devices

With different combinations of Pd and TiAu electrodes, the VO_2 devices can show tunable volatility enabled by different proton distributions across the channels after the selective hydrogenation. The TiAu + TiAu devices retain the pristine VO_2 channels and exhibit threshold switching with symmetric I-V hysteresis loops in both positive and negative bias polarities, as shown in Fig. 3A and fig. S11. V_{th}, above which the E-IMT is triggered by Joule heating due to the flowing current, and holding voltage (V_{hold}), below which the relaxation happens, are ±3.2 and ±1.5 V on average, respectively. The devices retain a clear gap between V_{th} and V_{hold} for reliable operation (figs. S12 and S13). The devices show stable volatile characteristics with no resistance changes after multicycle electric pulse stimuli are applied (Fig. S14). These results indicate that the TiAu + TiAu device can be used to emulate artificial neurons, and the well-known leaky integrate and fire (LIF) neuron functions are demonstrated, as shown in Fig. 3B. The TiAu + TiAu device is connected to a load resistor (R_L) in series and a capacitor (C_M) in parallel. Current pulses are applied to the circuit and once the potential across the TiAu + TiAu device reaches V_{th} through C_M charging, the device can be switched from the off-state to the on-state with a sudden increase of current flow (Fig. 3C). The firing rate is tunable upon the capacitor and the input current pulses [including pulse width (t_p), amplitude (A_p), and duty ratio (D_p)] (figs. S15 to S19). Apart from current pulses, voltage pulses are also effective to activate the LIF neuron circuit and to modulate the firing behavior (fig. S20).

On the other hand, the TiAu + Pd devices show a nonvolatile characteristic after the hydrogenation. As shown in Fig. 3D, there is a combination of nonvolatile resistive switching and volatile threshold switching (with a V_{th} of ~2.4 V) in the positive bias polarity of I-V curves even after 1000 sweeps. Considering that the undoped TiAu + Pd devices exhibit threshold switching only, this unique phenomenon should be attributed to the partially hydrogen-doped channels, which are a mixture of VO_2 and H_xVO_2. Because protons are able to drift in the channel under an external electric field, we can observe the changes of device resistance upon consecutive I-V sweeps and multicycle electric pulses, and the devices maintain their resistance states for $>10^4$ s after the removal of electrical stimuli (figs. S21 to S23). Such a nonvolatile feature widely exists in the doped TiAu + Pd devices with reasonable cycle-to-cycle and device-to-device variations (fig. S24).

The insertion of protons into the H_xVO_2 channels introduces intermediate resistance states to the hydrogenated TiAu + Pd devices, which can be used to design artificial synapses. As shown in fig. S25A, upon consecutive positive or negative electric pulse stimuli, device resistance and hence synaptic weight (w) can be repeatedly programmed. The change of device resistance is dependent on the applied voltage pulse amplitude and width. For example, when the pulse amplitude increases from 8 to 10 V/μm, the updated resistance after 50 consecutive pulses is doubled (Fig. 3E). When the pulse width increases from 1 to 10 μs, the resistance difference after 50 consecutive pulses reaches about nine times (fig. S25B). Under different pulse conditions, the TiAu + Pd devices perform a relatively linear resistance potentiation with an extracted nonlinear factor of ~0.8 (fig. S26). This is beneficial for the enhancement of training accuracy in spiking neural networks (SNNs) using the hydrogenated TiAu + Pd devices as synapses (*37*).

The multiple metastable states in the devices and their impact on the resistance states are elucidated by density functional first-principles calculations. Figure 3F shows the relative stability analysis based on the total energy differences between pseudomonoclinic H_xVO_2 (M1) and pseudorutile H_xVO_2 (R) phases with different concentrations of H dopants. The simulation results reveal that the pseudomonoclinic phase (light sea green region) is more favorable when x is $\lesssim$0.25 atomic fraction of a H_xVO_2 formula unit. Upon further doping, the pseudorutile phase becomes more stable (light magenta regime). By accessing the electronic properties in terms of the total and partial density of states (DOS) at different hydrogenation levels, we observe that the intermediately doped H_xVO_2 (R) phase retains a metallic characteristic with increasing H doping ($0.25 < x \leq 0.5$), while the increase of H content in the lightly doped H_xVO_2 (M1) phase reduces its bandgap before transitioning into this metallic state (fig. S27). The reduction of bandgap is attributed to the partial occupation of $d_{||}{}^*/\pi^*$ orbitals upon the addition of hydrogen and is reflected in the shifting down of the occupancy of $d_{||}$ (d_{x2-y2}) orbitals (fig. S28). Across the lightly hydrogenated TiAu + Pd device channels, there should be a portion of the semiconducting H_xVO_2 region with x value ranging between 0 and 0.25. Upon application of external electric field, the migration of protons results in the update of the x value in H_xVO_2 locally. Because the change of bandgap affects the resistivity of the semiconducting regions, their redistribution can bring about tunable intermediate resistance states to the synaptic devices.

Design and fabrication of cointegrated neural circuit motifs with $(H_x)VO_2$ devices

Through selective area doping, both volatile and nonvolatile $(H_x)VO_2$ devices can be integrated on a single chip (see Materials and Methods and fig. S29). Their interconnections allow the demonstration of feedforward excitation/inhibition neural circuits, which are fundamental micronetwork motifs. The circuit hardware primarily consists of a presynaptic neuron (N1), a postsynaptic neuron (N2), a synapse, and peripheral circuits (Fig. 4, A and B). The two neurons are connected in series through a synapse to control spiking signal transmission from N1 to N2 by adjusting the weight. To avoid detrimental voltage fluctuations due to signal interferences, operational amplifiers (op-amps) are introduced between neural components. Specifically, a voltage follower [i.e., isolator 1 (Iso1)] is placed between the N1 and the synapse (*38*), and an inverting amplifier plus a Howland current pump (*39*, *40*) for voltage-to-current conversion (i.e., Iso2) are installed between the synapse and the N2 (*41*). The synaptic weight (w) here is defined as the absolute value of the inverting amplifier's

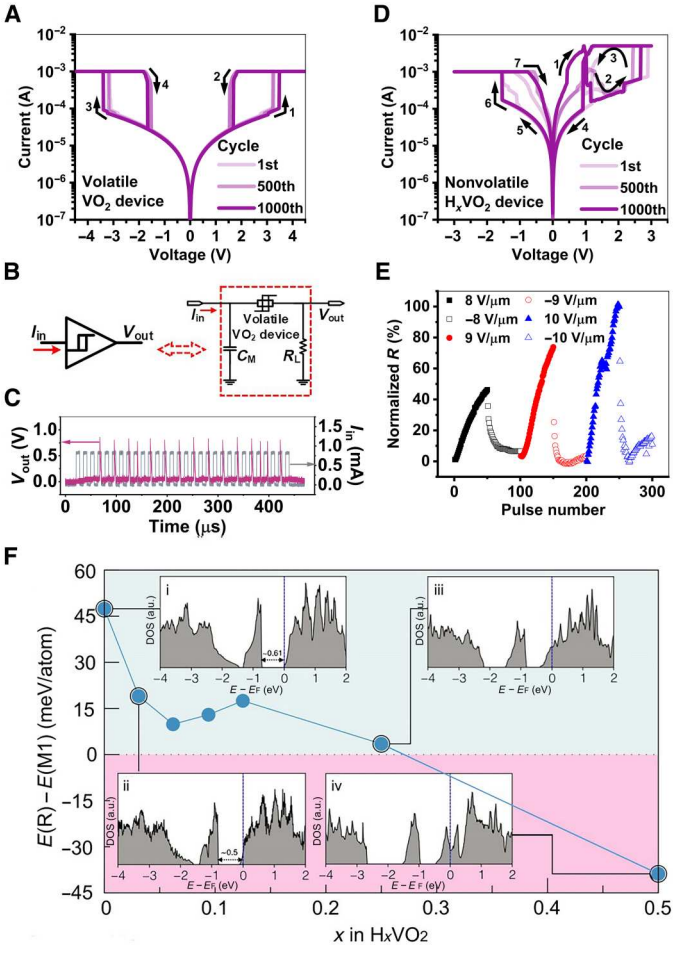

Fig. 3. Threshold switching and learning in $(H_x)VO_2$ devices. (**A**) *I-V* curves of the TiAu + TiAu device in the 1st, 500th, and 1000th sweep cycle with a compliance current (I_{cc}) of 1 mA. The TiAu + TiAu device clearly demonstrates volatile threshold switching. (**B**) Schematic of neuronal component composed of the volatile VO_2 device, a load resistor, and a capacitor. (**C**) Measured output voltage waveforms of the neuron. Amplitutde (A_p), capacitor (C_M), pulse width (t_p), and duty ratio (D_p) are set at 0.8 mA, 4.4 nF, 7 μs, and 50%, respectively. (**D**) *I-V* curves of the TiAu + Pd device in the 1st, 500th, and 1000th sweep cycle with an I_{cc} of 5 mA in the positive polarity and 1 mA in the negative polarity. The TiAu + Pd device exhibits a combination of nonvolatile resistive switching and threshold switching. (**E**) Potentiation and depression of the TiAu + Pd device upon different applied pulses. The pulse widths are 1 μs. (**F**) First-principles calculation of relative stabilities of H_xVO_2 (M1) and H_xVO_2 (R) phases across different levels of H concentrations. For the sake of clarity, H_xVO_2 (M1) and H_xVO_2 (R) are in pseudomonoclinic and pseudorutile phases, respectively, since the presence of protons alters the ideal lattice parameters and bond distances of both the pristine monoclinic and rutile phases. The light sea green region describes the zone where H_xVO_2 (M1) is more favorable, whereas the light magenta regime indicates that H_xVO_2 (R) is more stable. Insets (i), (ii), (iii), and (iv) are the total density of states (DOS) of the low-energy phases of 0.0, 0.03, 0.25, and 0.50 atomic fraction of H levels in H_xVO_2, respectively. With increasing H dopant level, the semiconducting monoclinic H_xVO_2 phase (i) narrows its bandgap from ~0.61 to 0.5 eV as seen in (ii). Upon further doping, it changes to metallic (iii) in its pseudomonoclinic phases and its pseudorutile phases (iv).

gain (i.e., the ratio of the resistance across the op-amp over the effective synapse resistance) (fig. S30). By tuning the input current pulses, we can directly modulate the spikes emanating from N1. Because of the existence of Iso1, the downstream synapse has little impact on N1, showcasing similar spiking characteristics under different synaptic weights (fig. S31). However, before transferring into N2, the ejected spike train needs to be processed by the synapse, so the firing of N2 is closely related to the synaptic weight. As shown in Fig. 4 (D and E), with the decrease (increase) of synaptic weight, the firing probability of N2 decreases (increases), indicating that the N2 behaves like an inhibitory (excitatory) neuron. The feedforward excitation/inhibition neural circuits are further simulated using Simulation Program with Integrated Circuit Emphasis (SPICE). The neuronal behavior can be well reproduced using an equivalent circuit consisting of a threshold switch and a capacitor (fig. S32). The simulated spiking behaviors of N1 and N2 under different synaptic weights and input current pulses are in good agreement with the results measured in hardware (Fig. 4C and fig. S33). The consistency of simulation and measurement results augment the credibility of recognition tasks that are executed in the $(H_x)VO_2$ neural networks. In this work, Iso1 and Iso2 were inserted in the connection between one synapse and one neuron, but it is not necessary to reserve an exclusive isolator for each synapse-neuron pair when the connection scales up (i.e., between multiple synapses and one neuron). These isolators can be shared by serving as a part of neuron peripheral circuitry wherein multiplexers and demultiplexers are included between adjacent neural layers and multiple synapses are connected in parallel.

$(H_x)VO_2$-based SNNs

To showcase the excitatory and inhibitory neural circuits using both volatile and nonvolatile $(H_x)VO_2$ devices in the context of network-level recognition tasks, an SNN was designed using the experimental data from the devices. SNNs use "spikes" and learning occurs by modulating the synaptic weights based on the relative timing of the spikes, known as spike timing–dependent plasticity (STDP) (*42*). The local, sparse, and unsupervised nature of STDP lends itself to low-power on-chip embedded intelligence applications. The network architecture for the SNN is shown in Fig. 1C. The network is made of volatile VO_2 neurons connected by nonvolatile H_xVO_2 synapses. In hardware implementations, such a system can be mapped to a cross-array of synapse devices, terminating at neuronal devices. The stochastic switching of the neuron was sigmoidal in nature (Fig. 4F). The linear potentiation of the H_xVO_2 was used in simulating the synaptic conductance change. We trained the network on the MNIST (*26*) and Fashion-MNIST (*27*) datasets, each consisting of 10 classes of 28-by-28 pixel grayscale images of handwritten digits and fashion products, respectively. Both datasets used in the simulations were composed of 60,000 training samples and 10,000 test samples. The inputs to the network were Poisson spike trains, generated from the image pixel values. In addition, for the Fashion-MNIST, the dataset was filtered using the Sobel filter for edge detection before converting to spikes. The simulated networks consisted of an input layer of size 784 (equivalent to the dimensionality of the input data), an excitatory layer, and an inhibitory layer of 1600 each for MNIST and 400 each for Fashion-MNIST. All the neurons in the excitatory layer are connected to all the neurons in the input layer with excitatory connections. The neurons in the inhibitory layer are connected to one

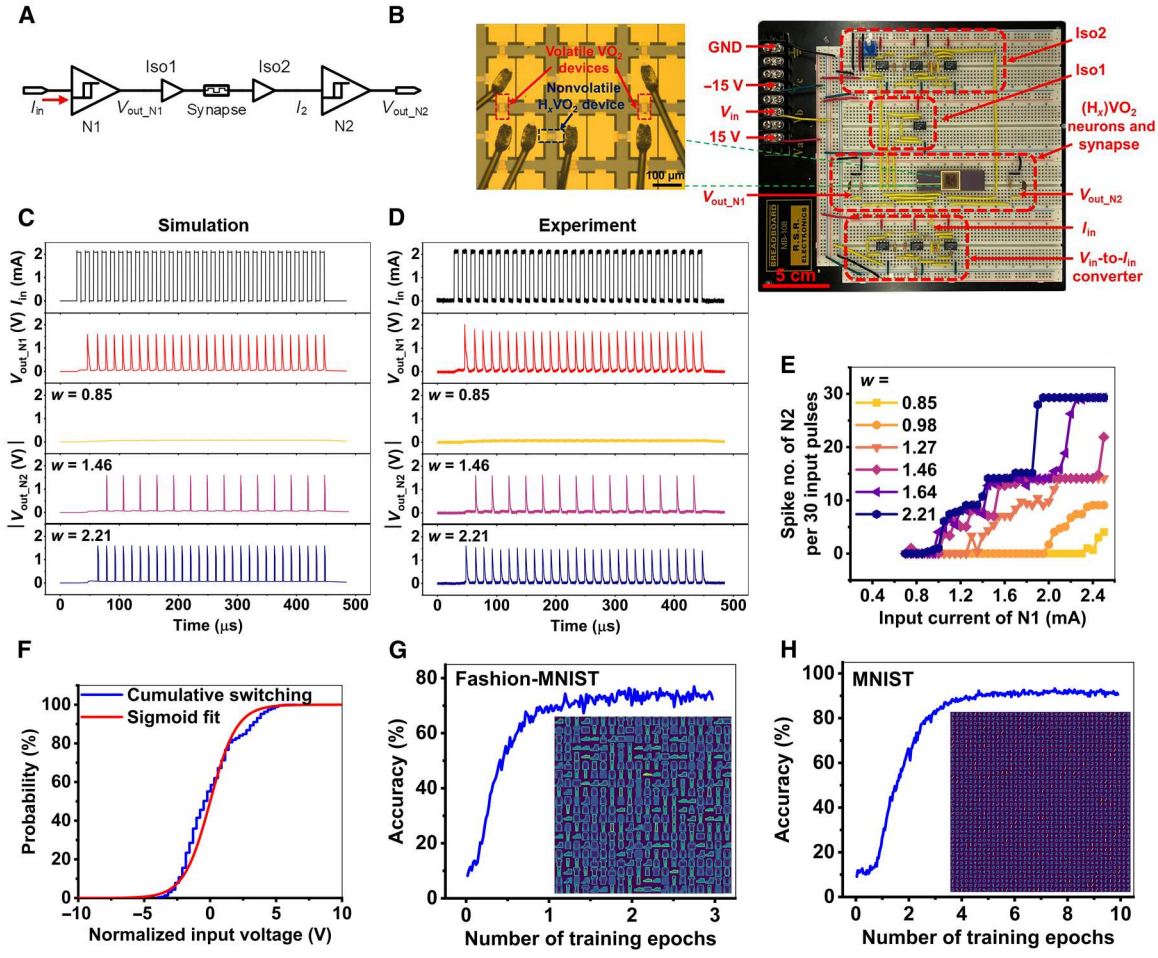

Fig. 4. $(H_x)VO_2$ neural circuits and SNNs. (**A**) Schematic of a connected neural circuit for the feedforward excitation and inhibition motifs. A presynaptic neuron (N1), a synapse, and a postsynaptic neuron (N2) are connected in series with two isolators inserted between them. (**B**) Photograph of the neural circuit hardware. Inset: Neuromorphic chip with both volatile neuron-like and nonvolatile synapse-like $(H_x)VO_2$ devices. GND stands for ground. A voltage-to-current converter is used to convert voltage pulses (V_{in}) from an arbitrary function generator into current pulses (I_{in}) as the circuit input. (**C**) Simulated and (**D**) measured output voltage waveforms of N1 and N2 for different synaptic weights. The current pulse train injecting into N1 has an A_p of 2.1 mA, a t_p of 7 μs, and a D_p of 50%. (**E**) Measured input-current–dependent firing probability (defined by the output spike number per 30 input current pulses) of N2 under different synaptic weights. (**F**) Cumulative switching dynamics of the volatile VO_2 neurons, which are fitted into sigmoidal stochastic switching neurons used in the network simulation. Training accuracy for (**G**) Fashion-MNIST and (**H**) MNIST over 3 and 10 training epochs, respectively. For Fashion-MNIST, we have a batch size of 16, while it is 32 for MNIST. For both datasets, each epoch consists of 60,000 training images. We obtained a final test accuracy of 73.22% on Fashion-MNIST and 92.1% on MNIST. Inset of (G) is the trained weight pattern for Fashion-MNIST. The network of 400 excitatory neurons was trained over the 60,000 training images for three epochs. Inset of (H) is the trained weight pattern for MNIST. The network of 1600 excitatory neurons was trained over the 60,000 training images for 10 epochs.

corresponding excitatory neuron with excitatory synapses and with inhibitory synapses to all the rest. The inhibitory connections achieve winner-take-all functionality in the SNN. The employment of the inhibitory connections greatly increases the generalization capability of the network, as shown in fig. S34. Note that only the excitatory connections from the input to the excitatory layer are tunable, while the other synaptic conductance remains static. Details of the network simulation can be found in Materials and Methods. After training, three independent test runs on the two datasets were performed. The simulated networks achieved an average test accuracy of 73.29% (SD: 0.09%) for Fashion-MNIST (Fig. 4G) and 92.26% (SD: 0.05%) for MNIST (Fig. 4H). These accuracies are in line with state-of-the-art unsupervised approaches for both datasets (*43*, *44*), demonstrating the efficacy of $(H_x)VO_2$ devices for scalable neuromorphic systems.

DISCUSSION

Selective area electron doping is demonstrated for archetypal Mott oxide electronic devices using insulator-metal transitions. This process enables monolithic integration of homotypic volatile threshold firing neurons and nonvolatile synapses for memory, providing a platform to implement Mott neuromorphic hardware for brain-inspired computing electronics and neural systems emulation studies. In the long term, the approach presented here can be of use to various emerging semiconductors that require heavy concentrations of dopants in device technologies.

MATERIALS AND METHODS

VO_2 thin-film deposition

Before deposition, 10-by-10 mm^2 c-plane sapphire substrates were cleaned through an ultrasonic bath of toluene, acetone, and isopropyl alcohol in sequence. The 50-nm-thick VO_2 thin films were deposited using an ultrahigh vacuum magnetron sputtering system from AJA International Inc. During deposition, a V_2O_5 ceramic target was used in the deposition powered with a radio frequency source at 100 W. The substrate temperature was 650°C. The chamber pressure was set at 5 mTorr of the Ar/O_2 mixture with a ratio of 99.9/0.1. The deposition rate was 0.6 nm/min. Before material characterizations, the H_xVO_2 samples were annealed at 200°C in a homebuilt furnace filled with a forming gas (5% H_2 balanced by 95% Ar) for 30 min.

(H_x)VO_2 device fabrication

Both volatile (TiAu + TiAu) and nonvolatile (TiAu + Pd) VO_2 devices were fabricated on a single sapphire substrate. After substrate cleaning and 50-nm-thick VO_2 thin-film deposition, the thin film was patterned using argon ion milling, during which SPR-220-3.5 photoresist served as a mask layer. Next, Ti (10 nm)/Au (100 nm) contact pads were formed through photolithography with LOR-3A and S1813 photoresists, electron beam evaporation (Ti deposition came first), and liftoff in Remover PG (Kayaku Advanced Materials,.Inc) at 80°C. To define the submicrometer channels, electron beam lithography was used in the next steps, where 495 poly(methyl methacrylate) (PMMA) A4 and 950 PMMA A4 were used as photoresists. Ti (10 nm)/Au (50 nm) stripes in the TiAu + TiAu and the TiAu + Pd devices were patterned by electron beam evaporation and liftoff in acetone at room temperature. The 50-nm-thick Pd electrode strips in the TiAu + Pd devices were patterned by repeating the processes for the TiAu electrode strips. The fabricated devices were annealed at 100°C in the forming gas with a flow rate of 50 standard cubic centimeter per minute to selectively hydrogenate the TiAu + Pd VO_2 device. For the feedforward excitation/inhibition neural circuits, the volatile and nonvolatile devices on the same chip were interconnected by further wire bonding to a chip carrier.

Electrical measurements

The electrical performance of (H_x)VO_2 device was characterized at room temperature by a Keithley 4200A-SCS parameter analyzer with ultrafast pulse measure units (4225-PMU) and remote preamplifier/switch modules (4225-RPM), which can apply submicrosecond electric pulses. For all electrical measurements, the TiAu electrode was connected to the ground. For (H_x)VO_2 neural circuits, in situ *I-V* measurement setups were designed and customized. The pulse trains applied across the circuits were generated by an arbitrary function generator (Tektronix AFG31000 Series), while the voltage signals were monitored using an oscilloscope (Tektronix DSOX4154A). A high-speed voltage-to-current converter was connected to the arbitrary function generator for applying microsecond current pulses to the (H_x)VO_2 neural circuits. For the neuronal behavior, the TiAu + TiAu VO_2 device was connected in series with a 200-ohm load resistor (R_L) and a 4.4-nF capacitor (C_M) in parallel. The voltage drops across the VO_2 device (V_{VO2}), and the R_L (V_{out}) were acquired from the oscilloscope. The current passing through the TiAu + TiAu VO_2 device was calculated with the equation $I = V_{out}/R_L$. For testing the individual neuron behavior in connected neuron-synapse-neuron circuits, customized isolators were used between the three components to avoid signal interferences among these devices, which might adversely affect signal propagation throughout the circuit.

Simulation methodology for neural circuits

Both single neuronal component and neural circuit behaviors were simulated with LTspice. The TiAu + TiAu VO_2 device was modeled as a threshold switch highlighted by a red dash box, as shown in fig. S32A. The off-state resistance (R_H) of the threshold switch was constant, while the on-state resistance (R_L) was controlled by the voltage across the threshold switch ($V_{in} - V_{out}$). Meanwhile, a minimum R_L (i.e., R_{min}) was imposed through the transition voltage (V_{sim}). If $V_{in} - V_{out} > V_{sim}$, then the on-state resistance would be directly assigned with R_{min}. If $V_{in} - V_{out} < V_{sim}$, then the relationship between R_L and $V_{in} - V_{out}$ follows an empirical formula acquired through fitting the *I-V* characteristic in fig. S32B; i.e., $R_L = 1000/[\alpha + \beta \times (V_{in} - V_{out}) + \gamma \times (V_{in} - V_{out})^2]$. The parameters for single neuronal component simulations are listed in table S1 and fig. S32D. In the neural circuit simulation, a programmable resistor serving as the synapse was connected between Iso1 and Iso2. Because pre- and postsynaptic neurons showed stochasticity, their parameters used in the simulation (table S2) were individually adjusted to fit their own behaviors better.

Simulation methodology for network-level recognition tasks

SNNs use bioplausible local learning mechanisms motivated by the propagation of electric impulses in the biological brain, often referred to as STDP (*45*, *46*). In STDP, the synaptic weights are modified in an exponential manner based on the relative timing difference between pre- and postsynaptic neuronal activities. The SNN implementation was done using a modified version of BindsNET (*47*), an open-source PyTorch-based framework. The network architecture was adopted from (*43*) for both the MNIST and Fashion-MNIST datasets. The stochastic neuron model with the VO_2 neuron dynamics was used. The linear potentiation of the H_xVO_2 synapse with four-bit discretization was taken. The weight dynamics is computed using synaptic traces (*48*), and the weight update rule is characterized by

$$\Delta w = \begin{cases} \eta_{post} \times \chi_{pre} \text{ on postsynaptic spike} \\ -\eta_{pre} \times \chi_{post} \text{ on presynaptic spike} \end{cases} \quad (1)$$

Here, χ_{pre} and χ_{post} are the pre- and postsynaptic traces, respectively, and are set to 1 whenever the pre- or postsynaptic neurons fire and decay exponentially to 0 with decay time constant τ_{trace}. η_{post}/η_{pre} represent the pre- and postsynaptic learning rates. To mimic quantized weight updates typically observed in such device technologies (*49*), the weights in the network-level simulations were quantized using

$$w_q = \frac{\text{round}[(2^N - 1) \times w]}{2^N - 1} \quad (2)$$

Here, w and w_q are the nonquantized and quantized weights, respectively, and N is the quantization precision. Lateral inhibition is implemented using the inhibition layer and its inhibitory

connections. To stop a single neuron from dominating the learning process, homeostasis was implemented by adaptively scaling the input to the stochastic neuron. The network parameters are given in table S3.

Supplementary Materials

This PDF file includes:

Supplementary Text
Figs. S1 to S34
Tables S1 to S3
References

REFERENCES AND NOTES

1. B. Yan, X. Cao, H. Li, paper presented at the 55th Annual Design Automation Conference, San Francisco, CA, 24 June 2018.
2. Y. Wang, K.-M. Kang, M. Kim, H.-S. Lee, R. Waser, D. Wouters, R. Dittmann, J. J. Yang, H.-H. Park, Mott-transition-based RRAM. *Mater. Today* **28**, 63–80 (2019).
3. M. S. Nikoo, R. Soleimanzadeh, A. Krammer, G. M. Marega, Y. Park, J. Son, A. Schueler, A. Kis, P. J. Moll, E. Matioli, Electrical control of glass-like dynamics in vanadium dioxide for data storage and processing. *Nat. Electron.* **5**, 596–603 (2022).
4. J. Lin, S. Sonde, C. Chen, L. Stan, K. Achari, S. Ramanathan, S. Guha, paper presented at 2016 IEEE International Electron Devices Meeting (IEDM), San Francisco, CA, 3 to 7 December 2016.
5. P.-Y. Chen, J.-S. Seo, Y. Cao, S. Yu, paper presented at 2016 IEEE/ACM International Conference on Computer-Aided Design (ICCAD), Austin, TX, 7 to 10 November 2016.
6. M. Jerry, W.-Y. Tsai, B. Xie, X. Li, V. Narayanan, A. Raychowdhury, S. Datta, paper presented at 2016 74th Annual Device Research Conference (DRC), Newark, DE, 19 to 22 June 2016.
7. E. Corti, J. A. Cornejo Jimenez, K. M. Niang, J. Robertson, K. E. Moselund, B. Gotsmann, A. M. Ionescu, S. Karg, Coupled VO_2 oscillators circuit as analog first layer filter in convolutional neural networks. *Front. Neurosci.* **15**, 628254 (2021).
8. M. D. Pickett, G. Medeiros-Ribeiro, R. S. Williams, A scalable neuristor built with Mott memristors. *Nat. Mater.* **12**, 114–117 (2013).
9. S. Oh, Y. Shi, J. Del Valle, P. Salev, Y. Lu, Z. Huang, Y. Kalcheim, I. K. Schuller, D. Kuzum, Energy-efficient Mott activation neuron for full-hardware implementation of neural networks. *Nat. Nanotechnol.* **16**, 680–687 (2021).
10. J. Park, C. Oh, J. Son, Anisotropic ionic transport-controlled synaptic weight update by protonation in a VO_2 transistor. *J. Mater. Chem. C* **9**, 2521–2529 (2021).
11. G. Li, D. Xie, H. Zhong, Z. Zhang, X. Fu, Q. Zhou, Q. Li, H. Ni, J. Wang, E.-j. Guo, M. He, C. Wang, G. Yang, K. Jin, C. Ge, Photo-induced non-volatile VO_2 phase transition for neuromorphic ultraviolet sensors. *Nat. Commun.* **13**, 1729 (2022).
12. Y. J. Lee, K. Hong, K. Na, J. Yang, T. H. Lee, B. Kim, C. W. Bark, J. Y. Kim, S. H. Park, S. Lee, H. W. Jang, Nonvolatile control of metal-insulator transition in VO_2 by ferroelectric gating. *Adv. Mater.* **34**, 2203097 (2022).
13. R. Yuan, Q. Duan, P. J. Tiw, G. Li, Z. Xiao, Z. Jing, K. Yang, C. Liu, C. Ge, R. Huang, Y. Yang, A calibratable sensory neuron based on epitaxial VO_2 for spike-based neuromorphic multisensory system. *Nat. Commun.* **13**, 3973 (2022).
14. Z. Wang, S. Joshi, S. Savel'ev, W. Song, R. Midya, Y. Li, M. Rao, P. Yan, S. Asapu, Y. Zhuo, H. Jiang, P. Lin, C. Li, J. H. Yoon, N. K. Upadhyay, J. Zhang, M. Hu, J. P. Strachan, M. Barnell, Q. Wu, H. Wu, R. S. Williams, Q. Xia, J. J. Yang, Fully memristive neural networks for pattern classification with unsupervised learning. *Nat. Electron.* **1**, 137–145 (2018).
15. Q. Duan, Z. Jing, X. Zou, Y. Wang, K. Yang, T. Zhang, S. Wu, R. Huang, Y. Yang, Spiking neurons with spatiotemporal dynamics and gain modulation for monolithically integrated memristive neural networks. *Nat. Commun.* **11**, 3399 (2020).
16. J. Woo, P. Wang, S. Yu, Integrated crossbar array with resistive synapses and oscillation neurons. *IEEE Electron Device Lett.* **40**, 1313–1316 (2019).
17. Y. Gong, H. Yuan, C.-L. Wu, P. Tang, S.-Z. Yang, A. Yang, G. Li, B. Liu, J. van de Groep, M. L. Brongersma, M. F. Chisholm, S.-C. Zhang, W. Zhou, Y. Cui, Spatially controlled doping of two-dimensional SnS_2 through intercalation for electronics. *Nat. Nanotechnol.* **13**, 294–299 (2018).
18. H.-P. Komsa, J. Kotakoski, S. Kurasch, O. Lehtinen, U. Kaiser, A. V. Krasheninnikov, Two-dimensional transition metal dichalcogenides under electron irradiation: Defect production and doping. *Phys. Rev. Lett.* **109**, 035503 (2012).
19. H. Fang, M. Tosun, G. Seol, T. C. Chang, K. Takei, J. Guo, A. Javey, Degenerate n-doping of few-layer transition metal dichalcogenides by potassium. *Nano Lett.* **13**, 1991–1995 (2013).
20. C. Ahn, A. Bhattacharya, M. Di Ventra, J. N. Eckstein, C. D. Frisbie, M. Gershenson, A. Goldman, I. Inoue, J. Mannhart, A. J. Millis, A. F. Morpurgo, D. Natelson, J.-M. Triscone, Electrostatic modification of novel materials. *Rev. Mod. Phys.* **78**, 1185–1212 (2006).
21. P. A. Lee, N. Nagaosa, X.-G. Wen, Doping a Mott insulator: Physics of high-temperature superconductivity. *Rev. Mod. Phys.* **78**, 17–85 (2006).
22. Y. Zhou, X. Guan, H. Zhou, K. Ramadoss, S. Adam, H. Liu, S. Lee, J. Shi, M. Tsuchiya, D. D. Fong, S. Ramanathan, Strongly correlated perovskite fuel cells. *Nature* **534**, 231–234 (2016).
23. H. Yoon, M. Choi, T.-W. Lim, H. Kwon, K. Ihm, J. K. Kim, S.-Y. Choi, J. Son, Reversible phase modulation and hydrogen storage in multivalent VO_2 epitaxial thin films. *Nat. Mater.* **15**, 1113–1119 (2016).
24. J. Wei, H. Ji, W. Guo, A. H. Nevidomskyy, D. Natelson, Hydrogen stabilization of metallic vanadium dioxide in single-crystal nanobeams. *Nat. Nanotechnol.* **7**, 357–362 (2012).
25. V. Andreev, V. Kapralova, V. Klimov, Effect of hydrogenation on the metal-semiconductor phase transition in vanadium dioxide thin films. *Phys. Solid State* **49**, 2318–2322 (2007).
26. Y. LeCun, C. C. Christopher, J.C. Burges, The MNIST database of handwritten digits (2010); http://yann.lecun.com/exdb/mnist/.
27. H. Xiao, K. Rasul, R. Vollgraf, Fashion-MNIST: a Novel Image Dataset for Benchmarking Machine Learning Algorithms (2017); https://arxiv.org/abs/1708.07747.
28. J. Chenavas, J. Joubert, J. Capponi, M. Marezio, Synthese de nouvelles phases denses d'oxyhydroxydes M^{3+} OOH des metaux de la premiere serie de transition, en milieu hydrothermal à tres haute pression. *J. Solid State Chem.* **6**, 1–15 (1973).
29. Y. Chen, Z. Wang, S. Chen, H. Ren, L. Wang, G. Zhang, Y. Lu, J. Jiang, C. Zou, Y. Luo, Non-catalytic hydrogenation of VO_2 in acid solution. *Nat. Commun.* **9**, 818 (2018).
30. P. Sermon, G. Bond, Hydrogen spillover. *Catal. Rev.* **8**, 211–239 (1974).
31. T. S. Kasırga, J. M. Coy, J. H. Park, D. H. Cobden, Visualization of one-dimensional diffusion and spontaneous segregation of hydrogen in single crystals of VO_2. *Nanotechnology* **27**, 345708 (2016).
32. X. Duan, S. T. White, Y. Cui, F. Neubrech, Y. Gao, R. F. Haglund, N. Liu, Reconfigurable multistate optical systems enabled by VO_2 phase transitions. *ACS Photonics* **7**, 2958–2965 (2020).
33. S. Chen, Z. Wang, L. Fan, Y. Chen, H. Ren, H. Ji, D. Natelson, Y. Huang, J. Jiang, C. Zou, Sequential insulator-metal-insulator phase transitions of VO_2 triggered by hydrogen doping. *Phys. Rev. B* **96**, 125130 (2017).
34. D. Delgado, G. Hefter, M. Minakshi, Hydrogen Generation, in *Alternative Energies* (Springer, 2013), pp. 141–161.
35. P. Schilbe, Raman scattering in VO_2. *Physica B Condens. Matter.* **316–317**, 600–602 (2002).
36. S. Zhang, J. Y. Chou, L. J. Lauhon, Direct correlation of structural domain formation with the metal insulator transition in a VO2 nanobeam. *Nano Lett.* **9**, 4527–4532 (2009).
37. P.-Y. Chen, B. Lin, I.-T. Wang, T.-H. Hou, J. Ye, S. Vrudhula, J.-S. Seo, Y. Cao, S. Yu, paper presented at 2015 IEEE/ACM International Conference on Computer-Aided Design (ICCAD), Austin, TX, 2 to 6 November 2015.
38. F.-X. Liang, I.-T. Wang, T.-H. Hou, Progress and benchmark of spiking neuron devices and circuits. *Adv. Intell. Syst.* **3**, 2100007 (2021).
39. I. M. Pandiev, Analysis and design of voltage-controlled current sources for a grounded load. *Int. J. Circuit Theory Appl.* **43**, 756–775 (2015).
40. A. Mahnam, H. Yazdanian, M. M. Samani, Comprehensive study of Howland circuit with non-ideal components to design high performance current pumps. *Measurement* **82**, 94–104 (2016).
41. Y. Fu, Y. Zhou, X. Huang, B. Dong, F. Zhuge, Y. Li, Y. He, Y. Chai, X. Miao, Reconfigurable synaptic and neuronal functions in a V/VOx/HfWOx/Pt memristor for nonpolar spiking convolutional neural network. *Adv. Funct. Mater.* **32**, 2111996 (2022).
42. G.-Q. Bi, M.-m. Poo, Synaptic modifications in cultured hippocampal neurons: Dependence on spike timing, synaptic strength, and postsynaptic cell type. *J. Neurosci.* **18**, 10464–10472 (1998).
43. P. U. Diehl, M. Cook, Unsupervised learning of digit recognition using spike-timing-dependent plasticity. *Front. Comput. Neurosci.* **9**, 99 (2015).
44. Q. Zhu, Z. Wang, An image clustering auto-encoder based on predefined evenly-distributed class centroids and MMD distance. *Neural Process Lett.* **51**, 1973–1988 (2020).
45. P. Ferré, F. Mamalet, S. J. Thorpe, Unsupervised feature learning with winner-takes-all based stdp. *Front. Comput. Neurosci.* **12**, 24 (2018).
46. S. R. Kheradpisheh, M. Ganjtabesh, S. J. Thorpe, T. Masquelier, STDP-based spiking deep convolutional neural networks for object recognition. *Neural Netw.* **99**, 56–67 (2018).
47. H. Hazan, D. J. Saunders, H. Khan, D. Patel, D. T. Sanghavi, H. T. Siegelmann, R. Kozma, BindsNET: A machine learning-oriented spiking neural networks library in python. *Front. Neurosci.* **12**, 89 (2018).
48. A. Morrison, M. Diesmann, W. Gerstner, Phenomenological models of synaptic plasticity based on spike timing. *Biol. Cybern.* **98**, 459–478 (2008).

49. S. Hu, G. Qiao, T. Chen, Q. Yu, Y. Liu, L. Rong, Quantized STDP-based online-learning spiking neural network. *Neural Comput. Appl.* **33**, 12317–12332 (2021).
50. S. Chen, Z. Wang, H. Ren, Y. Chen, W. Yan, C. Wang, B. Li, J. Jiang, C. Zou, Gate-controlled VO_2 phase transition for high-performance smart windows. *Sci. Adv.* **5**, eaav6815 (2019).
51. W. Yi, K. K. Tsang, S. K. Lam, X. Bai, J. A. Crowell, E. A. Flores, Biological plausibility and stochasticity in scalable VO_2 active memristor neurons. *Nat. Commun.* **9**, 4661 (2018).
52. J. P. Perdew, K. Burke, M. Ernzerhof, Generalized gradient approximation made simple. *Phys. Rev. Lett.* **77**, 3865–3868 (1996).
53. Y. Cui, S. Shi, L. Chen, H. Luo, Y. Gao, Hydrogen-doping induced reduction in the phase transition temperature of VO_2: A first-principles study. *Phys. Chem. Chem. Phys.* **17**, 20998–21004 (2015).
54. S. Manna, P. Gorai, G. L. Brennecka, C. V. Ciobanu, V. Stevanović, Large piezoelectric response of van der Waals layered solids. *J. Mater. Chem. C* **6**, 11035–11044 (2018).
55. J. E. Saal, S. Kirklin, M. Aykol, B. Meredig, C. Wolverton, Materials design and discovery with high-throughput density functional theory: The open quantum materials database (OQMD). *Jom* **65**, 1501–1509 (2013).
56. I. Štich, R. Car, M. Parrinello, S. Baroni, Conjugate gradient minimization of the energy functional: A new method for electronic structure calculation. *Phys. Rev. B* **39**, 4997–5004 (1989).

Acknowledgments

Funding: The microscopy characterization work at BNL was supported by Department of Energy Office (DOE) Basic Energy Sciences (BES), Materials Sciences and Engineering Division under contract DE-SC0012704. The network-level simulations performed using experimental device characteristics at Penn State was supported in part by the National Science Foundation grant CCF no. 1955815. We acknowledge ARO W911NF1920237 (characterization of VO_2 devices) and NSF Award 1904081 (film synthesis) for support. Work performed at the Center for Nanoscale Materials, a U.S. DOE Office of Science User Facility, was supported by the U.S. DOE, Office of BES, under contract no. DE-AC02-06CH11357. S.M. and S.K.R.S.S. acknowledge the support provided by the DOE, Office of Science, BES Data, Artificial Intelligence and Machine Learning at DOE Scientific User Facilities program (Digital Twins and Collaborative MLExchange). This research used resources of the National Energy Research Scientific Computing Center, a DOE Office of Science User Facility supported by the Office of Science of the U.S. DOE under contract no. DE-AC02-05CH11231. We acknowledge the computing resources provided on Fusion and Blues, high-performance computing clusters operated by the Laboratory Computing Resource Center (LCRC) at Argonne National Laboratory. **Author contributions:** S.D., T.J.P., and S.R. conceived the study. S.D., H.Y., and T.J.P. deposited the VO_2 thin films. S.D. and Q.W. fabricated the devices. H.Y. conducted the XRD, Raman, and C-AFM characterizations. S.D. and H.Y. measured the device characteristics and the neural circuit performance. H.Y. built the device model and conducted the neural circuit simulation. A.P. and Y.Z. performed the scanning transmission electron microscopy and electron energy-loss spectroscopy experiments and analyzed the results. S.M. and S.K.R.S.S. carried out the DFT calculations and analyzed the results. A.N.M.N.I. and A.S. simulated the network-level recognition tasks and analyzed the results. S.D., T.J.P., and S.R. prepared the manuscript. All authors participated in discussing the results and providing sections and comments for the manuscript. **Competing interests:** The authors declare that they have no competing interests. **Data and materials availability:** All data needed to evaluate the conclusions in the paper are present in the paper and/or the Supplementary Materials.

Submitted 18 August 2022
Accepted 16 February 2023
Published 17 March 2023
10.1126/sciadv.ade4838